



Amorphous quantum dots co-catalyst: Defect level induced solar-to-hydrogen production

Shuangyong Guo^{a,1}, Yujin Ji^{b,1}, Youyong Li^b, Hui Li^c, Pengfei An^d, Jing Zhang^d, Junqing Yan^{a,*}, Shengzhong (Frank) Liu^a, Tianyi Ma^{c,*}

^a Key Laboratory of Applied Surface and Colloid Chemistry, Ministry of Education, Shaanxi Engineering Lab for Advanced Energy Technology, School of Materials Science and Engineering, Shaanxi Normal University, Xi'an 710119, People's Republic of China

^b Institute of Functional Nano & Soft Materials (FUNSOM), Jiangsu Key Laboratory for Carbon-Based Functional Materials & Devices, Soochow University, Suzhou, Jiangsu 215123, People's Republic of China

^c School of Science, RMIT University, Melbourne, VIC 3000, Australia

^d Beijing Synchrotron Radiation Facility, Institute of High Energy Physics, Chinese Academy of Sciences, Beijing 100049, People's Republic of China



ARTICLE INFO

Keywords:

Amorphous CuO_x
Quantum dot
Co-catalyst
Photocatalytic water splitting
H₂ generation

ABSTRACT

Photocatalytic water splitting has been regarded as the most economical means for the production of green hydrogen. However, the conversion efficiency of photocatalytic water splitting is still low. Herein, a uniform dispersion of amorphous and nanosized CuO_x species is in-situ loaded on the surface of TiO₂ to form am-CuO_x/TiO₂, representing the first-of-its-kind amorphous quantum dots as the co-catalysts for photocatalytic process. Their CuO_x particles anchor on the surface of TiO₂ via bondings between the surface Ti and Cu as confirmed by X-ray absorption spectroscopy measurements. Notably, ultraviolet photoelectron spectroscopy coupled with density functional theory calculations indicates that the defect energy levels of CuO_x act as the collection centers of the electrons photogenerated by TiO₂. Therefore, the am-CuO_x/TiO₂ catalyst exhibits photocatalytic H₂ evolution rate of 19.14 μmol/h under LED-365 illumination with the record-breaking AQE value of 52.29 %. This work will enable the design of more efficient photocatalytic green H₂ evolution.

1. Introduction

Achieving carbon neutrality is conducive to the sustainable development of human society. Green hydrogen is considered to be one of the most efficient and clean energy sources for replacing traditional fossil fuels and accelerating the achievement of the carbon neutrality target [1–3]. Photocatalytic water splitting for hydrogen evolution is an effective approach for green hydrogen production because it uses only the abundant solar energy and water [4–10]. However, the conversion efficiency of photocatalytic water splitting is still low due to the limitations of the multi-step process in this reaction [11–13]. Loading the cocatalyst can prolong the life of the photogenerated carriers and increase the rates of their surface reaction, and thus has become the mainstream strategy for achieving high-efficiency photocatalytic water splitting for H₂ production [10,14–16].

In this context, noble-metal based cocatalysts have already been confirmed to be highly active for H₂ generation; however, their high cost

and low abundance limit their large-scale application [17–20]. Copper-based oxide cocatalysts have been widely studied as effective candidate materials for H₂ generation from photocatalytic water splitting, due to their abundant reserves and easy preparation [21–28]. Recent studies show that copper oxides will change during the photocatalytic water splitting. For example, it was reported that the oxides undergo a chemical transformation to generate metallic copper during the photocatalytic process and act as the H₂ evolution sites [25,26]. Meanwhile, other studies showed that the loaded CuO_x species were first leached out into the solution and then re-photodeposited onto the surface of the photocatalyst [23,24,27,28]. Although the chemical restructuring of copper oxides can promote the subsequent surface reduction reaction, i.e. H₂ generation, the change in the chemical states will consume the photogenerated electrons and thus lower the solar energy conversion efficiency. Thus, stable and efficient copper-based cocatalysts for efficient hydrogen production by photocatalytic water splitting are still needed.

* Corresponding authors.

E-mail addresses: junqingyan@snnu.edu.cn (J. Yan), tianyi.ma@rmit.edu.au (T. Ma).

¹ These authors contributed equally to this work.

Recently, quantum dots (QDs) have been reported to be effective for enhancing the catalytic performance due to their discrete band structures, strong interaction with supports and exposed metal active centers [29–36]. However, no amorphous QD-based cocatalysts have been reported. For photocatalysis, a disordered atomic arrangement has three potential advantages compared to the crystalline state: 1) promotion of the bonding between the loaded QDs and support which is beneficial for the chemical stability of QDs; 2) generation of surface point defects acting as the reaction sites; 3) inducing the formation of defect levels that are helpful for the migration of photogenerated carriers of the semiconductors to the cocatalysts.

Herein, we report an amorphous CuO_x ($0.5 < x < 1$) QD-based cocatalyst in-situ loaded onto the surface of TiO_2 (am- $\text{CuO}_x/\text{TiO}_2$) prepared by the solution method. Due to the special precursors of TiCl_4 and CuCl_2 , the solution environment is a weak acid that corrodes the CuO_x quantum dots to an amorphous state until a chemically stable state is reached. Under high temperature, pressure and acid environment, a strong interaction between CuO_x and TiO_2 is obtained through the bonding between the surface Ti and Cu as confirmed by X-ray absorption spectroscopy (XAS). The broken crystal structure of CuO_x gives rise to defect levels acting as the collection centers of the photogenerated electrons of TiO_2 . The synthesized am- $\text{CuO}_x/\text{TiO}_2$ sample exhibits the photocatalytic H_2 evolution rates of 40.1, 19.14, 4.07 and 1.41 $\mu\text{mol}/\text{h}$ under simulated sunlight, LED-365, LED-405 and LED-420 illumination, respectively. The apparent quantum efficiency (AQE) values under LED lamps were calculated as 52.29% (365 nm), 11.12% (405 nm) and 3.85% (420 nm), which are higher than the results previously reported for TiO_2 -based materials. This work can help design highly efficient, low-cost and super-stable photocatalytic water splitting cocatalysts.

2. Experimental section

2.1. Synthesis of bare TiO_2

Rutile TiO_2 was prepared by the hydrothermal method. In detail, titanium tetrachloride (TiCl_4) was added dropwise into ice water under agitation to prepare TiCl_4 aqueous solution with a concentration of ca. 1 mol L^{-1} . Then, TiCl_4 aqueous solution (30 mL) was mixed with anhydrous ethanol (10 mL). After stirring for 5 min, the solution was transferred to a 75 mL Teflon-lined autoclave for static crystallization at 180 °C for 4 h. The resulting precipitation after crystallization was separated from the liquid phase by centrifugation at 10,000 rpm for 10 min, and then was thoroughly cleaned with water and ethanol, and dried at 60 °C overnight. The obtained bare TiO_2 was used in the experiment after grinding in an agate mortar.

2.2. Synthesis of am- $\text{CuO}_x/\text{TiO}_2$

The preparation of am- $\text{CuO}_x/\text{TiO}_2$ was similar to that of bare TiO_2 except for the addition of copper chloride (CuCl_2). A certain amount of CuCl_2 was dissolved in anhydrous ethanol (10 mL), and then TiCl_4 aqueous solution (30 mL) was added and stirred for 5 min. Similarly, after the hydrothermal reaction, centrifugation, washing, drying and grinding, am- $\text{CuO}_x/\text{TiO}_2$ samples were finally obtained. TiO_2 samples with different CuO_x loadings are represented as am- $\text{CuO}_x/\text{TiO}_2\text{-X}$ (where X ranges from 2 to 10, indicating the mass percentage of CuO_x in the prepared am- $\text{CuO}_x/\text{TiO}_2$ photocatalyst). We note that the am- $\text{CuO}_x/\text{TiO}_2\text{-6}$ the sample is referred to as simply am- $\text{CuO}_x/\text{TiO}_2$.

2.3. Synthesis of reference $\text{Cu}_2\text{O}/\text{TiO}_2$

Reference $\text{Cu}_2\text{O}/\text{TiO}_2$ were prepared by a photodeposition method [28]. Bare TiO_2 was dispersed in the mixture of ethanol/water and stirred for 0.5 h after slow addition of the desired amount of $\text{Cu}(\text{NO}_3)_2\cdot 3\text{H}_2\text{O}$. The reaction cell was vacuumed for 30 min to remove the air in the solution and the system, and then was irradiated by a 300 W Xe lamp for

4 h. After centrifugation, washing, and drying at 60 °C overnight, the reference sample of $\text{Cu}_2\text{O}/\text{TiO}_2$ was obtained.

2.4. Characterization

Transmission electron microscopy (TEM) test was performed using an FEI Tecnai G2 F20 electron microscope at an acceleration voltage of 200 kV. Spherical aberration-corrected electron microscopy was carried out using a JEM-ARM200F electron microscope. Fourier transform infrared spectra (FTIR) were obtained using a Nicolet V70 instrument with KBr powder used as the background when testing. Diffuse reflectance ultraviolet-visible (UV-Vis) spectra of the studied samples were recorded in air with reference to BaSO_4 using a Hitachi-UH4150 spectrophotometer, and quasi-in-situ ultraviolet-visible near infrared (UV-Vis-NIR) absorption measurements were carried out on the same instrument. Typically, the sample was dropped by water-ethanol mixture and then illuminated by Xe lamp for approximately 5 min, and then transferred for the absorption measurement. The specific surface areas in this experiment were measured using an ASAP2460 instrument, and the samples were first pre-treated in N_2 atmosphere at 200 °C. X-ray diffraction (XRD) patterns of the samples were obtained using a Rigaku Smartlab diffractometer. The X-ray diffractometer parameters used in this experiment were: radiation in the 2θ range of 20°–80°; Cu target K_α X-ray ($\lambda = 1.54186 \text{ \AA}$); the step size: 0.02°; tube voltage: 40 KV; tube current: 30 mA. X-ray photoelectron spectra (XPS) were acquired using an ESCALAB Xi⁺ system (Thermo Fisher Scientific), the binding energy for all the elements under study was corrected by the value of C1s of 284.8 eV. Meanwhile, by using He I resonance line of He resonance lamp (photon energy 21.22 eV, wavelength 584 Å) as excitation source, the ultraviolet electron spectra (UPS) were obtained. Room-temperature photoluminescence (PL) and time-resolved fluorescence spectroscopy were carried out using a PerkinElmer LS55 fluorescence spectrophotometer. X-ray absorption fine structure (XAFS) experiments were performed at the 1W1B beamline of the Beijing Synchrotron Radiation Facility (BSRF). The storage ring runs at 2.0 GeV with a maximum electron current of approximately 450 mA. The energy range of the incident X-ray is tunable from 4 to 25 keV by fix-exit Si (111) double crystal monochromator. The absorption edge of the standard metal foils was used to calibrate the X-ray energy. The samples were ground into fine powers and then pressed into thin disks with a diameter of 10 mm. Ti K-edge and Cu K-edge X-ray absorption near edge structure (XANES)/extended X-ray absorption fine structure (EXAFS) spectra were collected at room temperature in the transmission mode. The electrochemical measurements were carried out in a conventional three-electrode cell using a CHI600E electrochemical workstation. The current density is normalized to the geometric area of the electrode, i.e. 1 cm^2 . The potential in this paper is calibrated to the reversible hydrogen electrode. The sweep speed of the linear sweep voltammetry was 1 $\text{mV}\cdot\text{s}^{-1}$ and the test temperature was 25 °C.

2.5. Photocatalytic hydrogen evolution

The photocatalytic hydrogen production activity was measured using a Perfectlight Labsolar-6A all-glass automatic online trace gas analysis system. Typically, a catalyst sample (100 mg) was suspended in 10 % methanol aqueous solution (100 mL) in the reaction cell, stirred evenly and vacuumed for 30 min to remove the air in the solution and the system. The entire experiment was carried out in a constant temperature ice bath (6 °C). Under irradiation, a GC-7920 gas chromatograph was used to collect hydrogen in the thermal conductivity detector (NaX zeolite column, Ar as carrier gas), and online detection was conducted every 30 min to quantitatively analyze the hydrogen production activity.

2.6. Computational details

All theoretical simulations were conducted under the framework of spin-polarized density functional theory (DFT) with the calculations carried out using the Vienna ab initio software package version 5.4.1 [37,38]. The electronic exchange and correlation interactions were described by the Perdew-Burke-Ernzerhof functional under the generalized gradient approximation [39]. We also used Grimme's DFT-D2 correction method to consider the effect of weak van der Waals interactions [40]. The (110) surface of rutile TiO₂ was cleaved from its bulk counterpart with loading of the CuO_x cluster. The cut-off energy for the plane wave basis set was set to 450 eV and geometry optimizations were carried out with the Brilloin zone sampling at the gamma point until the total energy and force were converged to 1E⁻⁴ eV and -0.03 eV/Å, respectively.

3. Results and discussions

3.1. Preparation and characterizations of am-CuO_x/TiO₂

Fig. 1a shows the preparation process of the am-CuO_x/TiO₂ sample. Typically, only TiCl₄ and CuCl₂ were used and added into an ethanol aqueous mixture that was then sealed into a reactor. Under the selected temperature, the heterogeneous nucleation generated the hydrochloric acid that was considered to carry out in-situ corrosion of the CuO_x nanoparticles [23,28]. Thus, the obtained CuO_x was transformed from crystalline to amorphous. After the hydrothermal treatment at high temperature, high pressure and acid solution conditions, the synthesized am-CuO_x/TiO₂ was hypothesized to have a strongly bonded and chemically stable structure with electron-rich exposed Cu sites due to surface copper defects. To confirm the absence of the Cu element doping into the TiO₂ lattice, in-situ UV-Vis absorption measurements were carried out during the hydrothermal process [41] with the results shown in **Fig. S1a**. Bare TiCl₄, CuCl₂ and the mixture solution were chosen (**Fig. S1b**). For bare TiCl₄, a typical Ti⁴⁺ absorption curve was found under a temperature of 20°C, however, the absorption spectra became irregular at the temperatures of 30 and 40 °C, suggesting that solids blocking the

passage of incident light were generated at these temperatures. For CuCl₂, there were no changes in the absorption peaks (253 and 850 nm) for the reaction temperatures from 30 to 80 °C, suggesting that only the coordination of Cu²⁺ changed with almost no heterogeneous crystallization. Meanwhile, for the mixture (TiCl₄ + CuCl₂), clearly irregular spectra were detected at the temperatures of 30 and 40 °C; however, the typical Cu²⁺ absorption peak (ca. 850 nm) showed no change even under the temperature of 80 °C. Moreover, the peak intensity was almost the same as that for the bare CuCl₂, confirming that TiO₂ was first crystallized at a relatively low temperature and that the Cu²⁺ ions did not participate in the crystallization. The role of ethanol was examined as shown in **Fig. S2**, and it was found that there were no peaks changes in the UV-Vis absorption using the aqueous solution only at the temperatures ranging from 30 to 90 °C. This suggests that the addition of ethanol can promote the heterogeneous crystallization of Ti⁴⁺ ions.

X-ray diffraction (XRD) refinement was further carried out to confirm the absence of Cu doping into the TiO₂ lattice during the solution preparation process. As shown in **Fig. 1b** and **Fig. S3a**, both the am-CuO_x/TiO₂ sample and the bare TiO₂ sample showed XRD peaks for the typical rutile TiO₂ phase [42,43], and no impurity peaks were detected. The corresponding crystal structure parameters based on the Rietveld full-spectrum fitting method were calculated as $a=b=4.6002 \text{ \AA}$ and $c=2.9596 \text{ \AA}$ for am-CuO_x/TiO₂, and $a=b=4.5992 \text{ \AA}$, $c=2.9594 \text{ \AA}$ for the reference bare TiO₂. These results suggested that no Cu ions were doped into the TiO₂ lattice, in agreement with the UV-Vis absorption spectra discussed above. **Fig. S3b** shown the calculated full width at half maximum (FWHM) values, and both of the samples showed the same value of 0.523°, confirming their equal particle size. Moreover, almost no peak shifts were detected, suggesting that the addition of Cu²⁺ ions did not influence the crystallization of TiO₂. The reference samples were synthesized by changing the amount of the loaded CuO_x (2 %, 4 %, 8 % and 10 %). All of the samples showed the same rutile TiO₂ XRD patterns with no other peaks found (**Fig. S4a**). Moreover, the magnified main peak at the 2 of ca. 27.3° had the same position but different FWHM value (**Fig. S4b**), further suggesting the absence of Cu doping into the lattice. The reference bare TiO₂ obtained using different amounts of ethanol also only showed XRD peaks for the rutile phase (**Fig. S5a**) with

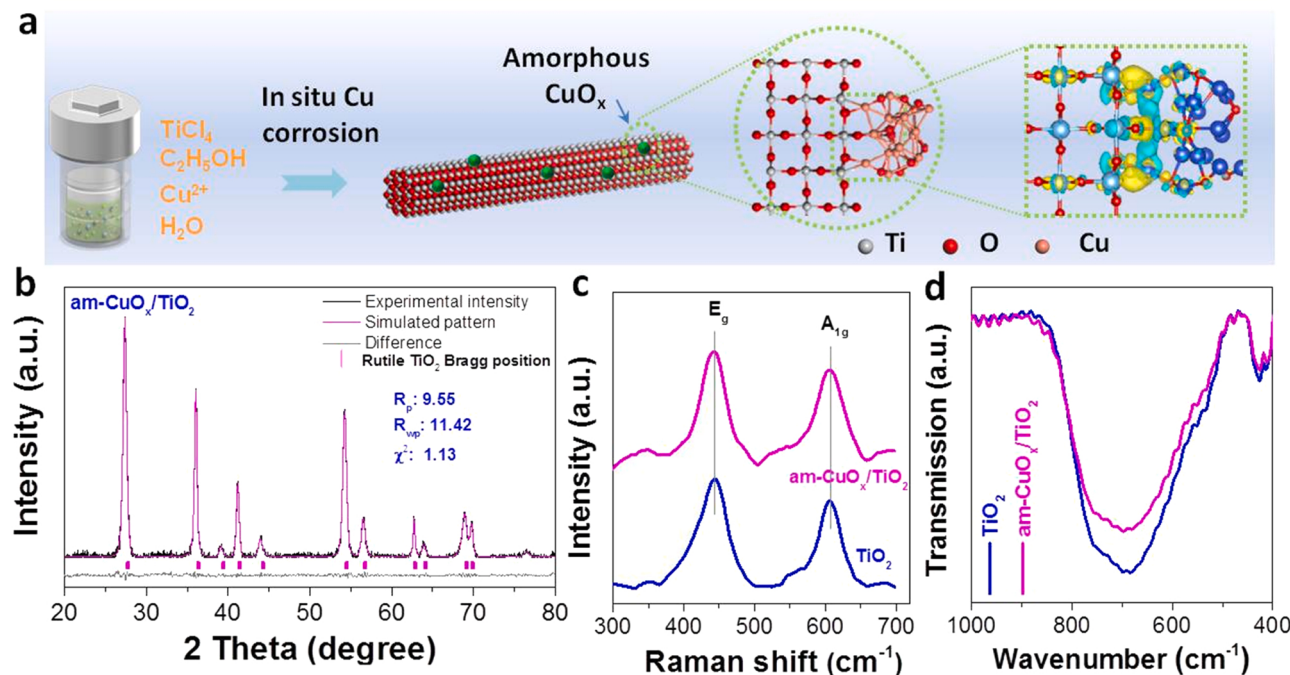


Fig. 1. (a) Schematic illustration of the preparation process of am-CuO_x/TiO₂, the atomic structure model is given with the corresponding charge distribution at the interface of CuO_x and TiO₂. (b) XRD refinement, (c) Raman and (d) FTIR results for the am-CuO_x/TiO₂ sample.

no shift in the main peak (Fig. S5b).

Raman spectroscopy was employed in the characterization of the TiO₂ and am-CuO_x/TiO₂ samples with the results shown in Fig. 1c. Two peaks located at ca. 445 and 610 cm⁻¹ that can be assigned to the symmetric stretching vibration i.e. the E_g mode and the antisymmetric bending vibration i.e. the A_{1g} mode of O-Ti-O bonds [42], are detected. The other reference samples of am-CuO_x/TiO₂ also gave similar Raman results (Fig. S6a). The ratio of the A_{1g} and E_g peak intensities was calculated to be 0.78 and > 0.8 for the TiO₂ and the am-CuO_x/TiO₂ samples, respectively (Fig. S6b), suggesting the enhancement of the O-Ti-O antisymmetric vibration. This means that the surface O-Ti-O bonding structure changes after CuO_x loading. The vibrational bands of the samples were further determined by the FTIR analysis. Both TiO₂ and am-CuO_x/TiO₂ give similar curves in the range of 400–1000 cm⁻¹ (Fig. 1d), the absorption band around 500–800 cm⁻¹ is assigned to the Ti-O bonds [44,45], and the intensity of am-CuO_x/TiO₂ is reduced relative to bare TiO₂, suggesting that the loaded CuO_x species can influence Ti-O bonds [44]. No peak shift was detected, confirming the absence of Cu ion doping [45]. Moreover, the typical surface -OH group signals at ca. 1636 and 3383 cm⁻¹ also showed lower intensities after CuO_x loading (Fig. S7), further suggesting the changed surface state of am-CuO_x/TiO₂.

O₂ temperature-programmed desorption (O₂-TPD) was carried out to explore the chemical states of the TiO₂ and am-CuO_x/TiO₂ samples, with the commercial Cu₂O used as the reference sample. As shown in Fig. S8, Cu₂O only gives one peak at ca. 423 °C, and the TiO₂-based samples show two clear peaks at ca. 240 and 430 °C that can be assigned to the weak adsorption by the surface defect sites and a chemical reaction with O₂, respectively. However, the am-CuO_x/TiO₂ sample showed a slightly

higher intensity compared to bare TiO₂ at ca. 432 °C, confirming the chemical change of loaded CuO_x. Meanwhile, the differences in the O₂-TPD peak locations between am-CuO_x/TiO₂ and Cu₂O suggest that the loaded CuO_x is different from the standard Cu₂O. Fig. S9 presents the N₂ adsorption desorption curves of the am-CuO_x/TiO₂ and TiO₂ samples that show the specific surface areas of 41.1 and 39.8 m²/g, respectively. The morphology and structure analyses were carried out by transmission electron microscopy (TEM). Bare TiO₂ shows the typical nanorod morphology (Fig. S10a), and under the dark-field condition, the surface is smooth (Fig. S10b). Similarly, clear lattice fringes were observed in the HRTEM image (Fig. S10c), and the corresponding interplanar spacing can be calculated as 0.32 nm (Fig. S10d) and is assigned to the (110) lattice plane of rutile TiO₂ [42]. The TEM images obtained under different goniometer tilts further suggest the nanorod structure (Fig. S11). Fig. 2a shows the TEM image of am-CuO_x/TiO₂ sample, showing the similar nanorod structure. However, the corresponding HRTEM image in Fig. 2b exhibits evenly distributed nanoparticles with uniform size loading on the surface of the nanorods, the corresponding particle size is statistically calculated to be in the range from 0.8 to 2.4 nm with an average size of 1.2 nm (Fig. S12), which is within the bounds of the quantum dot size. Magnification of the selected area does not show a clear lattice for the loaded particle, indicating that the loaded particles are amorphous. Meanwhile, the support TiO₂ shows an atomically resolved lattice (Fig. 2c). HRTEM images of other areas also show amorphous loaded CuO_x particles (Figs. S13–S14).

HRTEM images under the different goniometer tilts of – 5, 5, 15 and 25° were obtained to further confirm the amorphous state of the loaded CuO_x particles. As shown in Fig. 2d–e and Fig. S15, all of the results show clear lattice fringes of the support TiO₂, while no lattice fringes of CuO_x

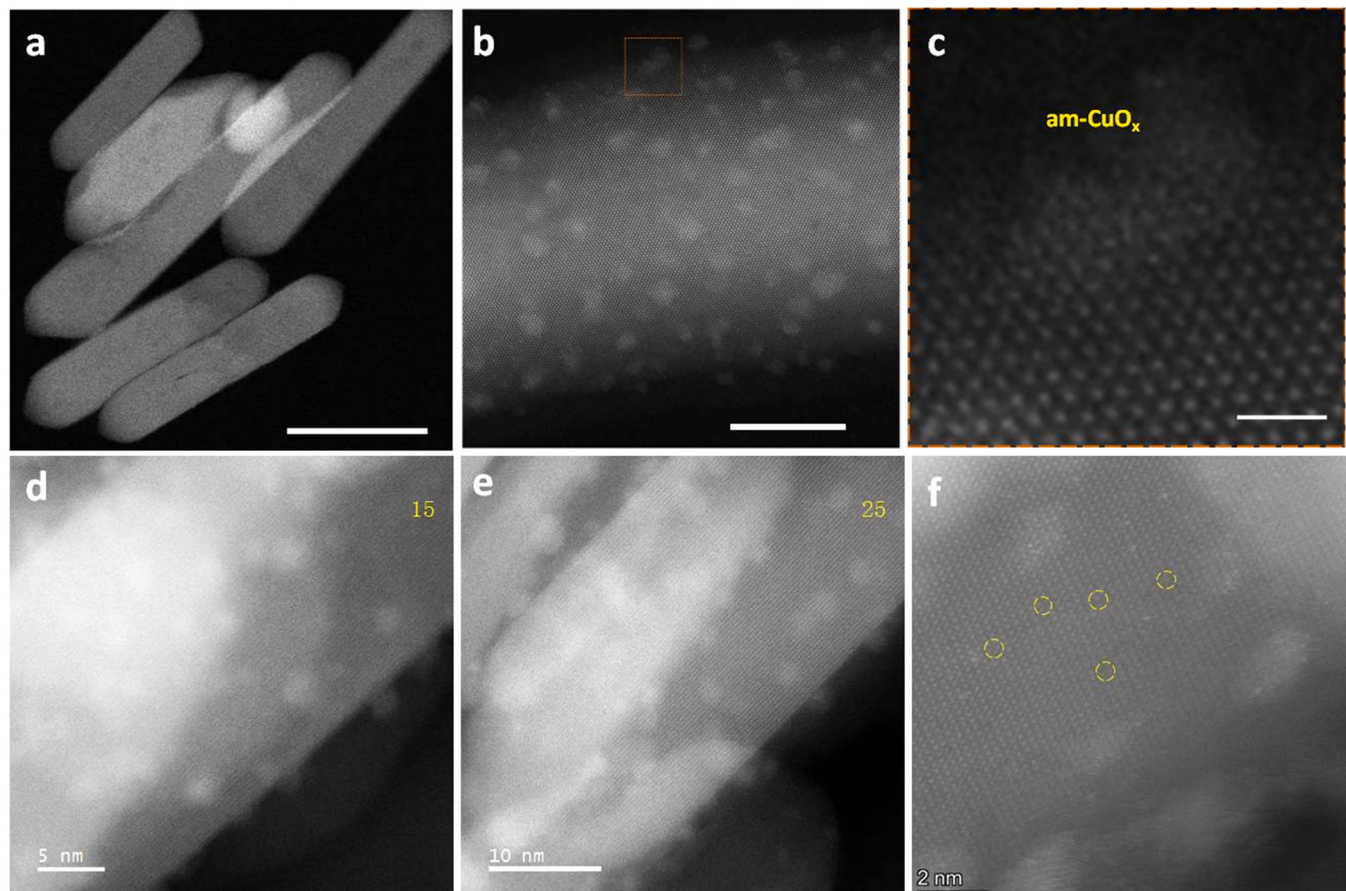


Fig. 2. Spherical aberration corrected electron microscope analysis under dark-field condition of the am-CuO_x/TiO₂ sample. (a) TEM image, scale bar, 50 nm; (b) HRTEM image, scale bar, 10 nm; (c) the corresponding magnified TEM image of the rectangle area in b marked in orange, scale bar, 1 nm; HRTEM images under the different goniometer tilts, (d) 15 and (e) 25°; (f) HRTEM image with the obvious point defect sites marked by yellow circles.

were detected under all four angles. Fig. S16 presents the elemental mapping results based on the TEM results. Clearly, the Ti and O are distributed evenly while the Cu distribution on the metal surface is discontinuous. The TEM images of the reference samples with different CuO_x amount loadings are also presented in Fig. S17. Clearly, all of the samples exhibit similar loading of nanoparticles, and the corresponding particle size distributions are also in the range from 0.8 to 2.4 nm. Meanwhile, some point defect sites near the loaded particles of am- $\text{CuO}_x/\text{TiO}_2$ were found (Fig. 2f), and bare TiO_2 samples give complete lattice fringes (Fig. S10c and S18), suggesting that CuO_x and TiO_2 interact.

The chemical valence state and coordination situation of the elements in am- $\text{CuO}_x/\text{TiO}_2$ sample were further studied by X-ray photoelectron spectroscopy (XPS) and X-ray absorption spectroscopy (XAS). As shown in Fig. 3a, the samples of bare TiO_2 and am- $\text{CuO}_x/\text{TiO}_2$ have two peaks at ca. 458.3 eV and 463.9 V in the Ti 2p XPS. These peaks were assigned to $2p_{3/2}$ and $2p_{1/2}$ of Ti^{4+} in TiO_2 [42,43], respectively. However, the obvious low binding energy shift of the $2p_{3/2}$ peak of am- $\text{CuO}_x/\text{TiO}_2$ (458.26 eV) compared to that of bare TiO_2 (458.38 eV) suggests the increased extranuclear electron density of the Ti element. Fig. S19 shows the Ti 2p XPS results for the reference am- $\text{CuO}_x/\text{TiO}_2$ samples and commercial rutile TiO_2 named $\text{TiO}_2\text{-ref}$. The shift of the Ti $2p_{3/2}$ peak (458.38 eV) of TiO_2 compared to 458.35 eV of $\text{TiO}_2\text{-ref}$, suggests the presence of some defect sites for the synthesized TiO_2 sample. On the other hand, all of the samples with CuO_x loading show low binding energy shifts compared to TiO_2 . The Cu 2p spectrum of am- $\text{CuO}_x/\text{TiO}_2$ shows peaks similar to those of the reference Cu_2O (Fig. 3b). Typically, the two peaks at ca. 932.2 eV and 952.1 eV can be

assigned to $2p_{3/2}$ and $2p_{1/2}$ of Cu^+ [26,28], respectively. Similarly, a slight shift can be detected for the $2p_{3/2}$ peaks from 932.2 eV of Cu_2O to 932.4 eV of am- $\text{CuO}_x/\text{TiO}_2$, confirming the reduced extranuclear electron density. The changed Ti and Cu binding energy may suggest the surface bonding between the Ti atoms and Cu atoms of the CuO_x particles. The reference loaded CuO_x samples exhibit similar Cu 2p XPS curves (Fig. S20a), and the Cu $2p_{3/2}$ peak shows a high binding energy shift (Fig. S20b). Fig. S21a presents the corresponding O 1 s XPS results of the samples under study. Two typical peaks at ca. 529.64 eV and 531.4 eV are found for all samples, and the first peak (529.64 eV) has been reported to be due to lattice oxygen, while the second peak is due to the surface -OH groups [7,42]. Fig. S21b presents the corresponding relative percentage of the -OH groups. Clearly, the CuO_x loading samples give the downward trend of the -OH group amount, in agreement with the above FTIR results (Fig. S7). Auger electron spectroscopy was further carried out to identify the electronic properties of the Cu element in the am- $\text{CuO}_x/\text{TiO}_2$ sample. It has been reported that the Cu Auger LMM transition of Cu_2O can only give one Auger peak, namely ${}^1\text{G}$, at the kinetic energy of 916.8 eV [46,47]. As shown in Fig. 3c, the reference Cu_2O sample shows the typical LMM Auger signal. However, the am- $\text{CuO}_x/\text{TiO}_2$ sample shows the peak at 916.5 eV, slightly lower than the value from the reference sample, suggesting that the chemical environment of Cu has been changed so that the loaded CuO_x is different from the standard Cu_2O .

X-ray absorption near-edge spectroscopy (XANES) was further performed to investigate the coordination environments of the Ti and Cu elements. Fig. S22a shows the Ti K-edge XANES results for the $\text{TiO}_2\text{-ref}$, TiO_2 and am- $\text{CuO}_x/\text{TiO}_2$ with all samples showing similar curves,

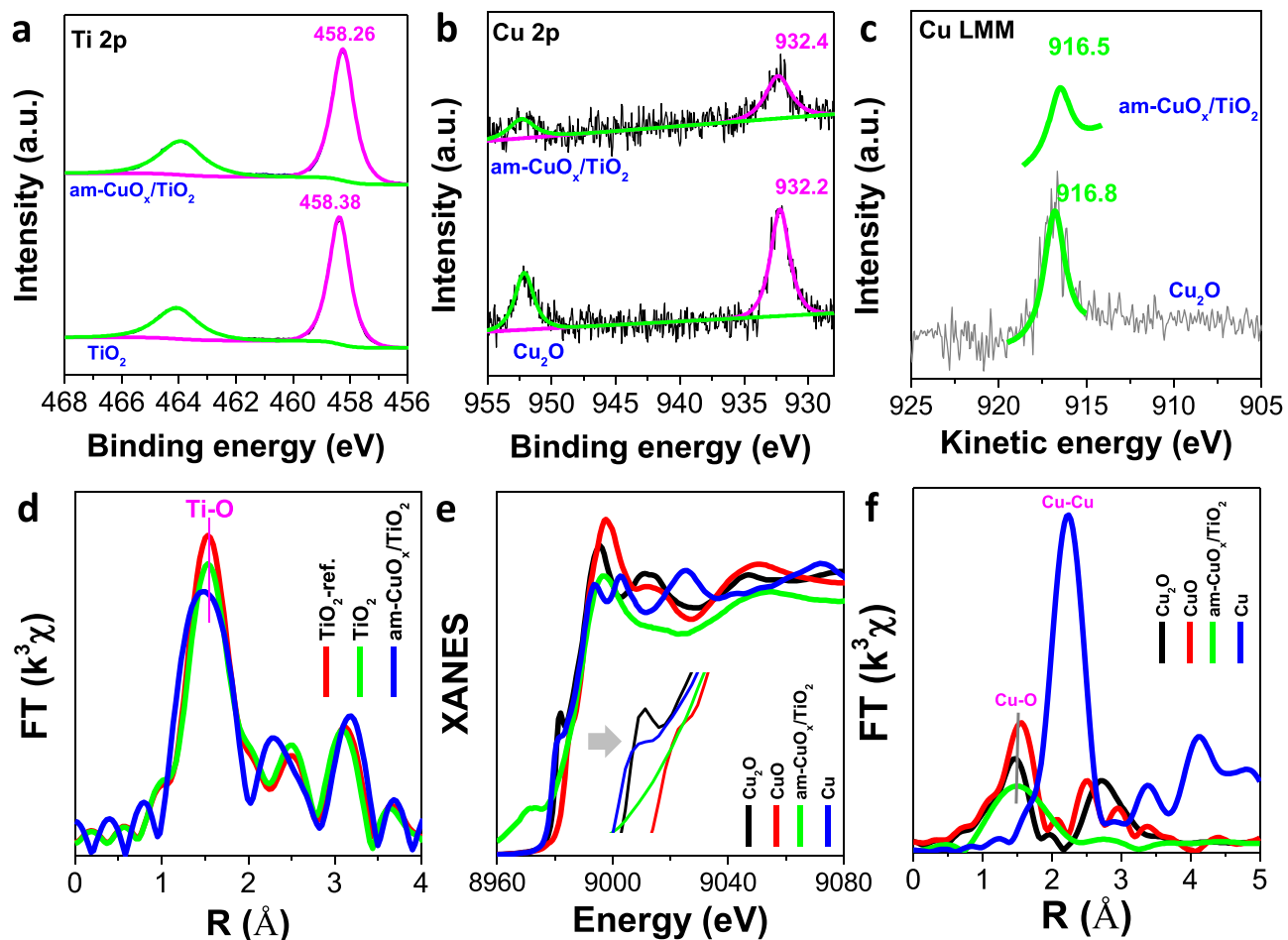


Fig. 3. Chemical valence state and coordination analysis of the am- $\text{CuO}_x/\text{TiO}_2$ sample. (a) Ti 2p XPS; (b) Cu 2p XPS; (c) Cu LMM AES; (d) Fourier-transformed Ti K-edge EXAFS spectra; (e) Cu K-edge XANES spectra; (f) Fourier-transformed Cu K-edge EXAFS spectra.

supporting that all of the samples are the rutile TiO_2 phase [29,48]. However, for the magnified XANES singles range from 4965 to 4975 eV (Fig. S22b), three peaks labeled A, B, and C can be detected, and the intensity of peak B increases from TiO_2 -ref. to TiO_2 and then to $\text{am-CuO}_x/\text{TiO}_2$, suggesting a greater number of point defect sites in the synthesized TiO_2 and $\text{am-CuO}_x/\text{TiO}_2$. It was reported that the increased intensity of peak B suggests that the central Ti atom site becomes more non-centrosymmetric [48,49]. Fig. 3d presents the corresponding Fourier transformed Ti K-edge extended X-ray absorption fine structure (EXAFS) result. The three samples exhibit the main peak at 1.5 Å ascribed to the Ti-O scattering path [48,49]. The intensities of this peak from highest to lowest are in the order TiO_2 -ref., TiO_2 and $\text{am-CuO}_x/\text{TiO}_2$, suggesting the decreased O coordination number of the Ti center of the synthesized samples.

Fig. 3e presents the Cu K-edge XANES results of the Cu, Cu_2O , CuO and $\text{am-CuO}_x/\text{TiO}_2$ samples with the distinct line shapes, indicating their different coordinated structures of elemental Cu. The pre-peaks as shown from the inset lines exhibit different position for the samples; in particular, $\text{am-CuO}_x/\text{TiO}_2$ is located between Cu_2O and CuO , confirming the X values to be in the region from 0.5 to 1. The corresponding EXAFS results can be found in Fig. 3f, and clearly show that the signals of the Cu-O bond at ca. 1.5 Å are different from each other. Typically, the $\text{am-CuO}_x/\text{TiO}_2$ sample not only exhibits a different peak position, but also a broadened peak, suggesting the formation of Ti-Cu bonding. Thus, the loaded CuO_x species is oxygen-deficient compared to Cu_2O and undergoes bonding with elemental Ti. Fig. S23 shows the proposed structure of the $\text{am-CuO}_x/\text{TiO}_2$ under study. Based on the results of HRTEM,

XPS, AES and XAFS, the loaded CuO_x particles own lots of unsaturated coordination of Cu, that is, they are the amorphous state.

3.2. Photocatalytic activity of $\text{am-CuO}_x/\text{TiO}_2$

The photocatalytic H₂ evolution performance was first evaluated under simulated sunlight illumination. As shown in Fig. 4a, all of the samples give linearly increasing amount of evolved H₂ with the $\text{am-CuO}_x/\text{TiO}_2$ sample showing the highest activity, followed by reference $\text{Cu}_2\text{O}/\text{TiO}_2$, TiO_2 and then TiO_2 -ref. with the corresponding H₂ evolution rates of 40.1, 16.1, 5.1 and 2.8 $\mu\text{mol}/\text{h}$ (Fig. S24a), respectively, suggesting that the loaded CuO_x particles can promote the separation and surface reaction of the photogenerated carriers. The reference samples with different am-CuO_x loading amounts also exhibit relatively high photocatalytic H₂ generation (Fig. S24b), further confirming the enhancement of the photogenerated electron-hole pair separation. The effect of the concentration of the photocatalyst in the reaction solution on the performance was examined. Clearly, 0.1 g photocatalyst gives the best performance (Fig. 4a and Fig. 4b). The visible-light driven photocatalytic H₂ evolution was further studied using LED lamps. As shown in Fig. 4c, the commercial rutile TiO_2 and the synthesized TiO_2 give almost no H₂ evolution, and the reference $\text{Cu}_2\text{O}/\text{TiO}_2$ shows observable albeit low H₂ evolution. Meanwhile, the $\text{am-CuO}_x/\text{TiO}_2$ sample exhibits the unique linearly increasing amount of generated H₂ with the increase in the reaction time. The corresponding H₂ evolution rates are given in Fig. S25a. The activity of $\text{am-CuO}_x/\text{TiO}_2$ under LED-420 was also measured as shown in Fig. S25b, and clearly shows the linearly

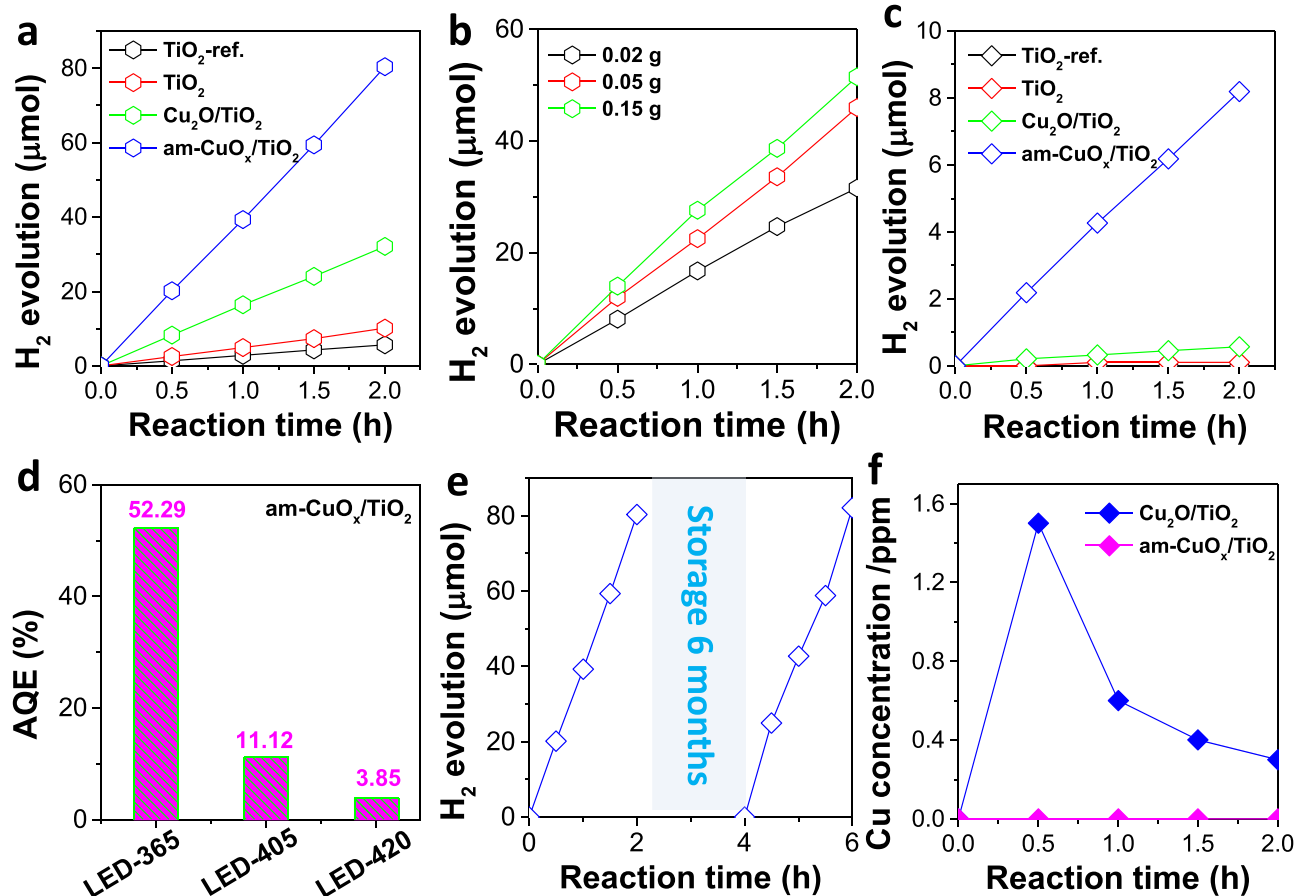


Fig. 4. Photocatalytic H₂ evolution performance. (a) The activity of the TiO_2 -ref., TiO_2 , $\text{Cu}_2\text{O}/\text{TiO}_2$ and $\text{am-CuO}_x/\text{TiO}_2$ samples under simulated sunlight illumination, catalysts, 0.1 g. (b) Photocatalytic H₂ evolution of $\text{am-CuO}_x/\text{TiO}_2$ under the different sample amount in 100 mL solution under simulated sunlight illumination. (c) The activity of the TiO_2 -ref., TiO_2 , $\text{Cu}_2\text{O}/\text{TiO}_2$ and $\text{am-CuO}_x/\text{TiO}_2$ samples under LED-405. (d) AQE values of the $\text{am-CuO}_x/\text{TiO}_2$ sample under LED-365, LED-405 and LED-420 illumination. (e) The stability measurement of the sample after storage for six months. (f) ICP-AES results of $\text{am-CuO}_x/\text{TiO}_2$ and reference $\text{Cu}_2\text{O}/\text{TiO}_2$ samples during the photocatalytic H₂ evolution. The reaction solution was taken out every half hour.

increasing activity with the H₂ evolution rate of 1.41 μmol/h (Fig. S25c). The visible light response originates from the surface defects [7,43]. It should be noted that the H₂ evolution rates under LED-365 and LED-405 illumination were 19.14 and 4.07 μmol/h (Fig. S25c), respectively. The corresponding apparent quantum efficiency (AQE) values were further calculated as 52.29 %, 11.12 % and 3.85 % under LED-365, LED-405 and LED-420 illumination, respectively, as given in Fig. 4d. Fig. S26 shows the comparison of AQE values of am-CuO_x/TiO₂ with the TiO₂-based samples reported in the literature. Clearly, am-CuO_x/TiO₂ exhibits the highest AQE values under both LED-365 (Fig. S26a) and LED-420 (Fig. S26b) illumination, further confirming that the surface-loaded amorphous CuO_x quantum dot particles not only strongly promote the separation of the photogenerated carriers of TiO₂, but also enhance the surface reaction rate of H₂ generation.

The chemical stability of am-CuO_x/TiO₂ sample is vital for its practical application. As shown in Fig. 4e, no activity change in the photocatalytic H₂ evolution occurs after the sample was stored for six months in air. Fig. S27 shows the cycle measurement with the same result of no activity change. The corresponding chemical elements analysis were further carried out by XPS after the cycle measurement. The Ti 2p (Fig. S28a), Cu 2p (Fig. S28b) and O 1s (Fig. S28c) spectra exhibit similar curves before and after the stability test; moreover, the relative percentage of the surface -OH signal at 531.4 eV is also unchanged (Fig. S28d). It was reported that the Cu₂O-based sample can be dissolved during photocatalytic water splitting [23,28]. The concentration of the Cu element in the reaction solution was detected by inductively coupled plasma-atomic emission spectrometry (ICP-AES) as shown in Fig. 4f. Clearly, the reference Cu₂O/TiO₂ exhibits similar dissolution phenomenon, and the am-CuO_x/TiO₂ sample shows no Cu signal in the solution.

The sub-nanometric size and strong bonding of the loaded CuO_x particles to the surface Ti and O endow am-CuO_x/TiO₂ with outstanding chemical stability.

3.3. Enhancement mechanism of am-CuO_x/TiO₂

Mechanism study of the amorphous CuO_x quantum dots promotion of the photocatalytic H₂ evolution was carried out through surface reaction and interface carriers migration analysis. As shown in Fig. 5, the surface was investigated by the electrochemical method. The polarization curves of TiO₂ and am-CuO_x/TiO₂ show an obvious difference, namely the overpotential is greatly reduced after the loading of CuO_x particles (Fig. 5a), suggesting that the surface CuO_x species are H₂ generation sites. Fig. S29 shows the corresponding Tafel slopes that are 102 mV/dec (am-CuO_x/TiO₂) and 180 mV/dec (TiO₂). The lowered Tafel slope indicates the high surface reaction rate. The polarization was further tested by adding the illumination by the LED-365 lamp under different powers. As we have reported previously, there are two contributions in the current response, namely the photo-current and the electric current [41]. Although no obvious change can be found in the total current signals (Fig. 5b), when the photo-current response is examined as shown in the inset, the signal increases with increased LED light power. More importantly, the photo-current values under the bias voltages of -0.12 and -0.13 V vs. RHE were determined as shown in Fig. 5c, and an almost linearly increasing current with increased LED light power can be obtained, suggesting that the surface CuO_x species can rapidly convert the incident photons. Electrochemical impedance spectroscopy (EIS) plots were used to evaluate the surface solid-liquid interface resistance. As shown in Fig. 5d, the TiO₂ and am-CuO_x/TiO₂

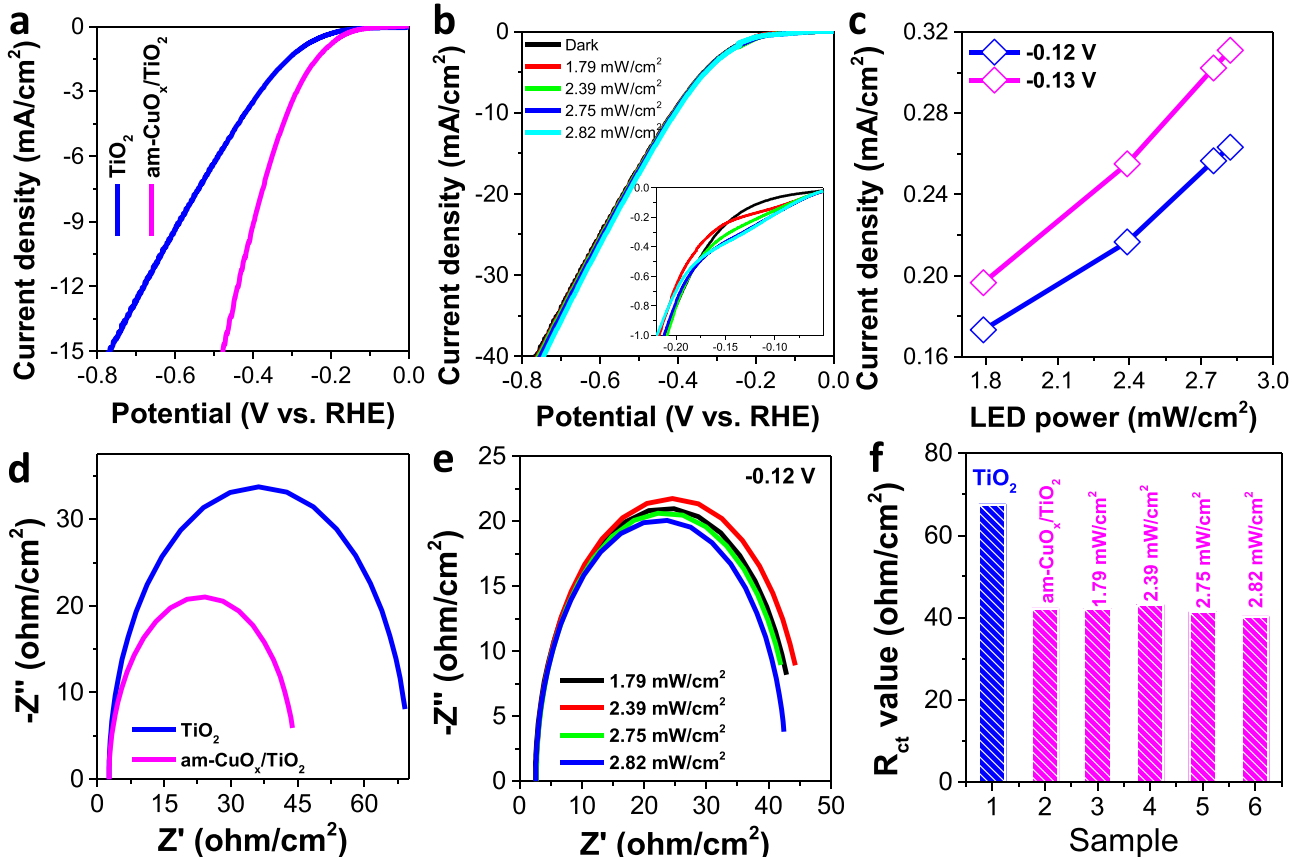


Fig. 5. Mechanism investigation: surface reaction study. (a) Polarization curves of TiO₂ and am-CuO_x/TiO₂; (b) polarization curves of am-CuO_x/TiO₂ under dark and LED-365 illumination with different power, the inset shows the main photocurrent response obtained from the amplified signals; (c) the corresponding photo-current response under bias voltage values of -0.12 and -0.13 V vs. RHE; (d) EIS plots of TiO₂ and am-CuO_x/TiO₂, (e) EIS plots of am-CuO_x/TiO₂ under different LED power; (f) the corresponding fitted R_{ct} values, 1: TiO₂, 2–6: am-CuO_x/TiO₂. All measurements were carried out in 0.5 M Na₂SO₄ solution.

samples display similar semicircles, and experiments with the above LED-365 illumination with different powers were further carried out, showing little change in the EIS results (Fig. 5e). Fig. S30 shows the circuit diagram for impedance fitting, where R_s , R_{ct} and CPE are the solution resistance, interfacial migration resistance and interfacial capacitance [50], respectively. In the present work, we only focus on R_s and R_{ct} . Table S1 shows that the fitted R_s values were ca. 2.6 ohm/cm², confirming the same reaction solution. Fig. 5f gives the corresponding obtained R_{ct} results. Typically, the bare TiO₂ and am-CuO_x/TiO₂ samples give the R_{ct} of 67.5 and 42.1 ohm/cm², respectively, under dark, indicating that the surface CuO_x loading can promote the interface migration of the carriers. However, the R_{ct} values under LED lamp illumination with different powers are almost the same as those obtained in the dark, confirming the chemically stable structure of am-CuO_x/TiO₂. Combining these results with the above-described photo-current response results (Fig. 5c), the loaded CuO_x particles can be considered as the bridge for the transfer of the photogenerated carriers between the catalyst and the solution.

The migration of the photogenerated carriers at the interface was studied by *quasi-in-situ* UV-Vis-NIR absorption spectroscopy, time-resolved photoluminescence (TRPL) spectroscopy and density functional theory (DFT) calculations. As shown in Fig. 6a, bare TiO₂ exhibits a typical rutile UV-Vis-NIR absorption curve with a cutoff band edge of 410 nm [7,42], whereas the UV-Vis-NIR spectrum for the am-CuO_x/TiO₂ sample shows a clear difference from the bare TiO₂ spectrum. Typically, absorption is observed in the visible-light range from 410 to 590 nm that can be assigned to the surface bonding between TiO₂ and CuO_x that gives rise to defect absorption. Moreover, near-infrared (NIR) absorption is observed in the range from 640 to 1000 nm that can be attributed to the light absorption by the loaded CuO_x species [51,52]. Photocatalytic H₂ evolution under LED-880 illumination was carried out but almost no activity was detected (Fig. S31). When the two samples were wetted by ethanol-water solution and then treated by illumination [7], significant changes were detected in the UV-Vis-NIR absorption curves (the insets in Fig. 6a). On bare TiO₂, only the Ti³⁺ signal after the treatment is observed arising from the reaction between the surface Ti⁴⁺ and the photogenerated electrons. While almost no Ti³⁺ signal can be discovered for the am-CuO_x/TiO₂ sample, the absorption of CuO_x is clearly enhanced, confirming that the surface CuO_x sites are the collection

centers of the photogenerated electrons of TiO₂ and lead to increased absorption via resonance absorption [53]. Fig. S32 displays the UV-Vis-NIR absorption spectra of the reference am-CuO_x/TiO₂ samples, and it is observed that the intensity of the broad peak ranging from 640 to 1000 nm increases with increasing amount of loaded CuO_x.

The room-temperature steady state photoluminescence (PL) spectra presented in Fig. S33 show that the am-CuO_x/TiO₂ sample exhibits lower PL intensity than the bare TiO₂, confirming the inhibition of the photogenerated carriers recombination by the loaded CuO_x nanoparticles. The corresponding time-resolved PL spectra show markedly different decay signals for the TiO₂ and am-CuO_x/TiO₂ samples (Fig. 6b), and the fitting results are shown in Table S2. The lifetime parameters of τ_1 and τ_2 are related to bulk and surface recombination, and A_1 and A_2 are the corresponding relative proportions. Thus, the increased lifetime of the photogenerated electrons in the bulk and the shortened lifetime at the surface suggest the transfer of electrons to the surface-loaded CuO_x particles. The average lifetimes τ_{avg} are 0.369 and 1.316 ns for the bare TiO₂ and am-CuO_x/TiO₂ samples, further confirming the electron-withdrawing effect of the CuO_x particles.

Fig. 6c shows the atomic structure model used for DFT calculations and Fig. 6d shows the corresponding projected density of states (PDOS) obtained for the am-CuO_x/TiO₂ sample with the clear highest occupied molecular orbital (HOMO) and lowest unoccupied molecular orbital (LUMO) of TiO₂. Meanwhile, CuO_x exhibits the obvious defect level above the LUMO of TiO₂. Thus, TiO₂ can generate electron-hole pairs under illumination, and the electrons will jump to the HOMO and then transfer to the defect level of CuO_x, where they participate in the water reduction reaction. The work function difference ($\Delta\phi$) was further analyzed to examine the surface band bending of the conduction band (CB) and the valence band (VB) of TiO₂ after contacting CuO_x. As shown in Fig. S34, the two TiO₂ and am-CuO_x/TiO₂ samples exhibit distinct cutoff band edge positions, and the corresponding $\Delta\phi_1$ is calculated to be $(17.88-3.75)-(17.45-3.35)=0.03$ eV, suggesting that there is only a slight ϕ upshift of am-CuO_x/TiO₂ compared to bare TiO₂. However, for the reference Cu₂O/TiO₂, the $\Delta\phi_2$ is 0.16 eV compared to TiO₂ (Fig. S35). Cu₂O has been reported to be a semiconductor with a relatively small W in comparison to TiO₂ [54,55], so that upon contact with TiO₂, its ϕ will shift down while that of TiO₂ will shift up, so that the integrated ϕ shifts upward (Fig. S36). The small magnitude of $\Delta\phi_1$

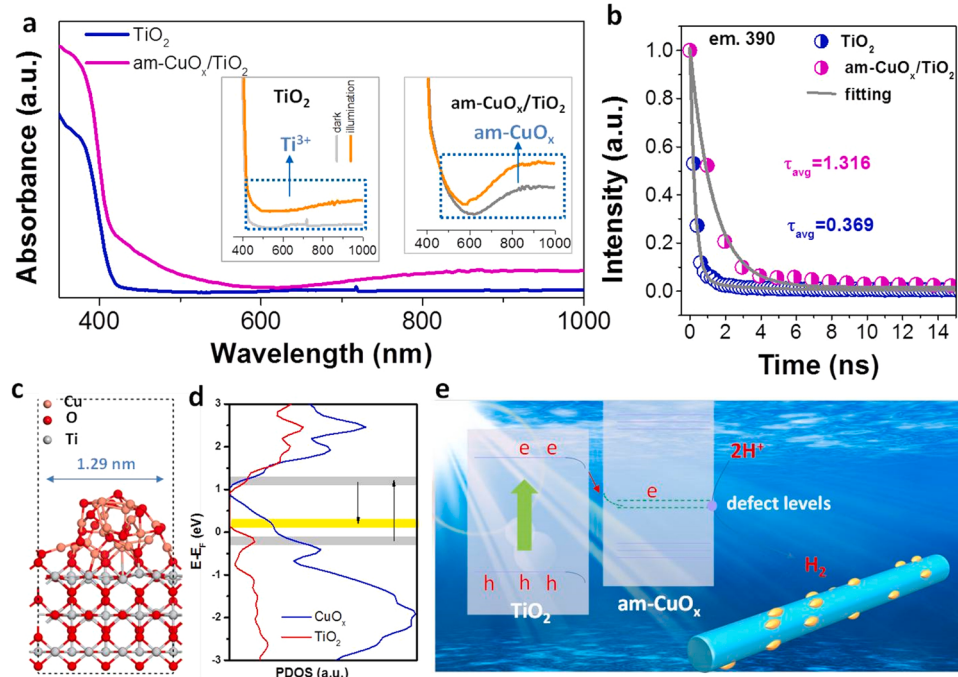


Fig. 6. Mechanism investigation: interface carrier migration study. (a) UV-Vis-NIR absorption spectrum of TiO₂ and am-CuO_x/TiO₂, the insets show the *quasi-in-situ* experiment results obtained from the illumination treatment of wetted samples by ethanol-water solution. (b) TRPL spectra (ex.: 295 nm). (c) Atomic model of the sample of am-CuO_x/TiO₂, (d) the corresponding PDOS curve, where the gray areas represent the HOMO and LUMO distribution of TiO₂ and the yellow area is the defect level of CuO_x, the migration pathway of photogenerated electrons from CB of TiO₂ to the defect level is also shown. (e) Schematic diagram of photocatalytic H₂ evolution of am-CuO_x/TiO₂.

suggests that there are defect levels below the Fermi level of CuO_x that can act as the collection centers of the photogenerated electrons of TiO₂ and also suggest the weak semiconductor property of loaded CuO_x. For a rutile TiO₂ nanorod, two main lattice planes of (100) and (110) are exposed (Fig. S37) with the relatively low surface energies (Table S3), and the corresponding ϕ values are calculated as 7.25 and 6.75 eV (Fig. S38), respectively. Thus, there is the internal driving force for the photogenerated electrons to migrate across the different lattice planes. The separated electrons will transfer to the surface CuO_x sites and then will carry out the H₂ evolution reaction (Fig. 6e).

4. Conclusions

Herein, the amorphous, low-cost and quantum-dot-sized photocatalytic H₂ evolution cocatalyst CuO_x species was reported that was obtained by the one-pot solution method in the synthesis of the am-CuO_x/TiO₂ sample. The in-situ UV-Vis absorption spectrum was used to detect the heterogeneous crystallization and showed that TiO₂ was generated first, followed by the generation of the CuO_x particles. Together with the XRD refinement results, the absorption spectra also suggested that no Cu element was doped into the TiO₂ lattices. Spherical aberration corrected HRTEM confirmed the amorphous state of the loaded CuO_x particles with an average particle size of ca. 1.2 nm. The binding energy shift in the XPS results confirmed the strong interaction between the Ti and Cu elements and the XAS results further suggested the bonding of surface Ti and Cu.

The am-CuO_x/TiO₂ sample exhibited an enhanced photocatalytic activity with the corresponding H₂ evolution rates of 40.1, 19.14, 4.07 and 1.41 μmol/h under the illumination by simulated sunlight, LED-365, LED-405 and LED-420, respectively. The AQE values under the above three LED lamp illumination conditions were calculated to be 52.29 %, 11.12 % and 3.85 %, which were all higher than the values for the TiO₂-based samples reported in the literature. The photocurrent response based on the polarization curves under LED-365 illumination with different power gave linearly increasing signals with increased power, confirming that the surface CuO_x particles were the H₂ generation sites and, the EIS plots suggested that the CuO_x were the stable transfer bridge between the catalyst and solution. Quasi-in-situ UV-Vis-NIR absorption spectrum further confirmed that the surface CuO_x sites were the collection centers of the photogenerated electrons of TiO₂. TRPL spectra and DFT calculations suggested the electron-withdrawing effect and the defect level of the CuO_x particles. Thus, the excellent carriers separation and surface reaction rate give rise to the enhanced photocatalytic H₂ evolution performance. This work can help design new low-cost and efficient photocatalytic cocatalysts as well as providing a thorough understanding of the photogenerated carriers' migration.

CRediT authorship contribution statement

Shuangyong Guo: Preparation, creation and presentation of the published work. **Yujin Ji:** Preparation, creation and presentation of the published work, specifically writing the initial draft. **Youyong Li:** Conducting a research and investigation process, specifically performing the experiments, and data/evidence collection. **Hui Li:** Conducting a research and investigation process, specifically performing the experiments, and data/evidence collection. **Pengfei An:** Conducting a research and investigation process, specifically performing the experiments, and data/evidence collection. **Jing Zhang:** Conducting a research and investigation process, specifically performing the experiments, and data/evidence collection. **Junqing Yan:** formulation of overarching research goals and aims, revise manuscript, acquisition of the financial support for the project leading to this publication. **Shengzhong (Frank) Liu:** formulation of overarching research goals and aims, revise manuscript, acquisition of the financial support for the project leading to this publication.

Declaration of Competing Interest

The authors declare that they have no known competing financial interests or personal relationships that could have appeared to influence the work reported in this paper.

Data availability

Data will be made available on request.

Acknowledgements

We acknowledge support from the Natural Science Foundation of China (No. 22072081), and the Fundamental Research Funds for the Central Universities (GK202201003), National Science Basic Research Plan in Shaanxi Province of China (2023-JC-JQ-16). P. An and J. Zhang acknowledge support from the National Key Research and Development Program of China (2017YFA0403400). T. Ma acknowledges Australian Research Council (ARC) through Future Fellowship (FT210100298), Discovery Project (DP220100603), and Linkage Project (LP210200504) schemes.

Appendix A. Supporting information

Supplementary data associated with this article can be found in the online version at doi:10.1016/j.apcatb.2023.122583.

References

- [1] N. AbouSeada, T.M. Hatem, Climate action: prospects of green hydrogen in Africa, Energy Rep. 8 (2022) 3873–3890.
- [2] H. Pan, M. Sun, X. Wang, M. Zhang, M. Murugananthan, Y. Zhang, A novel electric-assisted photocatalytic technique using self-doped TiO₂ nanotube films, Appl. Catal., B 307 (2022), 121174.
- [3] Y. Zhou, R.Y. Li, Z.X. Lv, J. Liu, H.J. Zhou, C.M. Xu, Green hydrogen: a promising way to the carbon-free society, Chin. J. Chem. Eng. 43 (2022) 2–13.
- [4] V. Kumaravel, S. Mathew, J. Bartlett, S.C. Pillai, Photocatalytic hydrogen production using metal doped TiO₂: a review of recent advances, Appl. Catal. B 244 (2019) 1021–1064.
- [5] D.M. Tobaldi, K. Kočí, M. Edelmannová, L. Lajaunie, B. Figueiredo, J.J. Calvino, M. P. Seabra, J.A. Labrincha, Cu_xO and carbon-modified TiO₂-based hybrid materials for photocatalytically assisted H₂ generation, Mater. Today Energy 19 (2021), 100607.
- [6] S. Jayachitra, D. Mahendiran, P. Ravi, P. Murugan, M. Sathish, Highly conductive NiSe₂ nanoparticle as a co-catalyst over TiO₂ for enhanced photocatalytic hydrogen production, Appl. Catal. B 307 (2022), 121159.
- [7] L. Chen, X.-L. Song, J.-T. Ren, Z.-Y. Yuan, Precisely modifying Co₂P/black TiO₂ S-scheme heterojunction by in situ formed P and C dopants for enhanced photocatalytic H₂ production, Appl. Catal. B 315 (2022), 121546.
- [8] K. Villa, J.R. Galan-Mascaros, N. Lopez, E. Palomares, Photocatalytic water splitting: advantages and challenges, Sustain. Energy Fuels 5 (2021) 4560–4569.
- [9] M. Wen, K. Mori, Y. Kuwahara, T. An, H. Yamashita, Design and architecture of metal organic frameworks for visible light enhanced hydrogen production, Appl. Catal. B 218 (2017) 555–569.
- [10] G. Zhang, Y. Xu, C. He, P. Zhang, H. Mi, Oxygen-doped crystalline carbon nitride with greatly extended visible-light-responsive range for photocatalytic H₂ generation, Appl. Catal. B 283 (2021), 119636.
- [11] Y. Zhang, J. Zhao, H. Wang, B. Xiao, W. Zhang, X. Zhao, T. Lv, M. Thangamuthu, J. Zhang, Y. Guo, J. Ma, L. Lin, J. Tang, R. Huang, Q. Liu, Single-atom Cu anchored catalysts for photocatalytic renewable H₂ production with a quantum efficiency of 56%, Nat. Commun. 13 (2022) 58.
- [12] G. Jia, Y. Wang, X. Cui, H. Zhang, J. Zhao, L.H. Li, L. Gu, Q. Zhang, L. Zheng, J. Wu, Q. Wu, D.J. Singh, W. Li, L. Zhang, W. Zheng, Wet-chemistry hydrogen doped TiO₂ with switchable defects control for photocatalytic hydrogen evolution, Matter 5 (2022) 206–218.
- [13] K.K. M. N. G. V.K. V, S.V. B, S. B, V. A, Improved H₂ yields over Cu-Ni-TiO₂ under solar light irradiation: behaviour of alloy nano particles on photocatalytic H₂O splitting, Appl. Catal. B 299 (2021), 120654.
- [14] N.N. Rosman, R.M. Yunus, N.R.A.M. Shah, R.M. Shah, K. Arifin, L.J. Minggu, N. A. Ludin, An overview of co-catalysts on metal oxides for photocatalytic water splitting, Int. J. Energy Res. 46 (2022) 11596–11619.
- [15] Y. Wang, M. Zhou, Y. He, Z. Zhou, Z. Sun, In situ loading CuO quantum dots on TiO₂ nanosheets as cocatalyst for improved photocatalytic water splitting, J. Alloy. Compd. 813 (2020), 152184–152184.
- [16] M. Esmat, H. El-Hosainy, R. Tahawy, W. Jevasuwan, N. Tsunoji, N. Fukata, Y. Ide, Nitrogen doping-mediated oxygen vacancies enhancing co-catalyst-free solar

photocatalytic H₂ production activity in anatase TiO₂ nanosheet assembly, *Appl. Catal. B* 285 (2021), 119755.

[17] Y. Wang, L. Mino, F. Pellegrino, N. Homs, P. Ramírez de la Piscina, Engineered Mo_x/TiO₂ interfaces for efficient noble metal-free photocatalytic hydrogen production, *Appl. Catal. B* 318 (2022), 121783.

[18] J. Liu, Y. Li, X. Zhou, H. Jiang, H.G. Yang, C. Li, Positively charged Pt-based cocatalysts: an orientation for achieving efficient photocatalytic water splitting, *J. Mater. Chem. A* 8 (2020) 17–26.

[19] Z. He, J. Fu, B. Cheng, J. Yu, S. Cao, Cu₂(OH)₂CO₃ clusters: novel noble-metal-free cocatalysts for efficient photocatalytic hydrogen production from water splitting, *Appl. Catal. B* 205 (2017) 104–111.

[20] Y. Wu, X. Chen, J. Cao, Y. Zhu, W. Yuan, Z. Hu, Z. Ao, G.W. Brudvig, F. Tian, J. C. Yu, C. Li, Photocatalytically recovering hydrogen energy from wastewater treatment using MoS₂@TiO₂ with sulfur/oxygen dual-defect, *Appl. Catal. B* 303 (2022), 120878.

[21] M. Zhang, R. Sun, Y. Li, Q. Shi, L. Xie, J. Chen, X. Xu, H. Shi, W. Zhao, High H₂ evolution from quantum Cu(II) nanodot-doped two-dimensional ultrathin TiO₂ nanosheets with dominant exposed {001} facets for reforming Glycerol with multiple electron transport pathways, *J. Phys. Chem. C* 120 (2016) 10746–10756.

[22] Y. Lin, S. Yang, Y. Liu, S. Zhang, H. Wang, H. Yu, F. Peng, In-situ photo-deposition CuO_{1-x} cluster on TiO₂ for enhanced photocatalytic H₂-production activity, *Int. J. Hydrol. Energy* 42 (2017) 19942–19950.

[23] S. Obregón, M.J. Muñoz-Batista, M. Fernández-García, A. Kubacka, G. Colón, Cu-TiO₂ systems for the photocatalytic H₂ production: influence of structural and surface support features, *Appl. Catal. B* 179 (2015) 468–478.

[24] D. Spanu, A. Minguzzi, S. Recchia, F. Shahvardanfarid, O. Tomanec, R. Zboril, P. Schmuki, P. Ghigna, M. Altomare, An operando X-ray absorption spectroscopy study of a NiCu–TiO₂ photocatalyst for H₂ evolution, *ACS Catal.* 10 (2020) 8293–8302.

[25] V. Polliotto, S. Livraghi, A. Krukowska, M.V. Dozzi, A. Zaleska-Medynska, E. Sellì, E. Giannello, Copper-Modified TiO₂ and ZrTiO₄: Cu oxidation state evolution during photocatalytic hydrogen production, *ACS Appl. Mater. Interfaces* 10 (2018) 27745–27756.

[26] Z. Xi, C. Li, L. Zhang, M. Xing, J. Zhang, Synergistic effect of Cu₂O/TiO₂ heterostructure nanoparticle and its high H₂ evolution activity, *Int. J. Hydrol. Energy* 39 (2014) 6345–6353.

[27] M. Jung, J.N. Hart, J. Scott, Y.H. Ng, Y. Jiang, R. Amal, Exploring Cu oxidation state on TiO₂ and its transformation during photocatalytic hydrogen evolution, *Appl. Catal. A Gen.* 521 (2016) 190–201.

[28] J. Liu, M. Liu, X. Yang, H. Chen, S.F. Liu, J. Yan, Photo-redeposition synthesis of bimetal Pt-Cu co-catalysts for TiO₂ photocatalytic solar-fuel production, *ACS Sustain. Chem. Eng.* 8 (2020) 6055–6064.

[29] Y. Yan, C.Y. Liu, H.W. Jian, X. Cheng, T. Hu, D. Wang, L. Shang, G. Chen, P. Schaaf, X.Y. Wang, E.J. Kan, T.R. Zhang, Substitutionally dispersed high-oxidation CoO_x clusters in the lattice of rutile TiO₂ triggering efficient Co-Ti cooperative catalytic centers for oxygen evolution reactions, *Adv. Funct. Mater.* 31 (2021), 2009610.

[30] G. Zuo, Y. Wang, W.L. Teo, Q. Xian, Y. Zhao, Direct Z-scheme TiO₂-ZnIn₂S₄ nanoflowers for cocatalyst-free photocatalytic water splitting, *Appl. Catal., B* 291 (2021), 120126.

[31] X. Cheng, Y. Lu, L. Zheng, M. Pupucevski, H. Li, G. Chen, S. Sun, G. Wu, Engineering local coordination environment of atomically dispersed platinum catalyst via lattice distortion of support for efficient hydrogen evolution reaction, *Mater. Today Energy* 20 (2021), 100653.

[32] D. Pan, Z. Han, Y. Miao, D. Zhang, G. Li, Thermally stable TiO₂ quantum dots embedded in SiO₂ foams: characterization and photocatalytic H₂ evolution activity, *Appl. Catal., B* 229 (2018) 130–138.

[33] H.V. Dang, Y.H. Wang, J.C.S. Wu, Z-scheme photocatalyst Pt/GaP-TiO₂-SiO₂: Rh for the separated H₂ evolution from photocatalytic seawater splitting, *Appl. Catal. B* 296 (2021), 120339.

[34] N.L. Reddy, S. Emin, V.D. Kumari, S. Muthukonda, Venkatakrishnan, CuO quantum dots decorated TiO₂ nanocomposite photocatalyst for stable hydrogen generation, *Ind. Eng. Chem. Res.* 57 (2018) 568–577.

[35] H. Zhang, P. Zhang, M. Qiu, J. Dong, Y. Zhang, X.W.D. Lou, Ultrasmall MoO_x clusters as a novel cocatalyst for photocatalytic hydrogen evolution, *Adv. Mater.* 31 (2019), e1804883.

[36] T. Qiu, L. Wang, B. Zhou, Y. Zhu, C. Zhuang, Q. Liu, Q. Shen, Y. Xiong, Y. Zhou, Z. Zou, Molybdenum sulfide quantum dots decorated on TiO₂ for photocatalytic hydrogen evolution, *ACS Appl. Nano Mater.* 5 (2021) 702–709.

[37] J. Kresse, J. Furthmüller, Efficient iterative schemes for ab initio total-energy calculations using a plane-wave basis set, *Phys. Rev. B Condens. Matter* 54 (1996) 11169–11186.

[38] G. Kresse, J. Furthmüller, Efficiency of ab-initio total energy calculations for metals and semiconductors using a plane-wave basis set, *Comput. Mater. Sci.* 6 (1996) 15–50.

[39] J.P. Perdew, K. Burke, M. Ernzerhof, Generalized gradient approximation made simple, *Phys. Rev. Lett.*, 77, 3865 (1996), *Phys. Rev. Lett.*, 78 (1997) 1396–1396.

[40] T. Kerber, M. Sierka, J. Sauer, Application of semiempirical long-range dispersion corrections to periodic systems in density functional theory, *J. Comput. Chem.* 29 (2008) 2088–2097.

[41] Y. Yang, Y. Ji, G. Li, Y. Li, B. Jia, J. Yan, T. Ma, S.F. Liu, IrO_x@In₂O₃ heterojunction from individually crystallized oxides for weak-light-promoted electrocatalytic water oxidation, *Angew. Chem. Int. Ed.* 60 (2021) 26790–26797.

[42] J. Yan, G. Wu, N. Guan, L. Li, Z. Li, X. Cao, Understanding the effect of surface/bulk defects on the photocatalytic activity of TiO₂: anatase versus rutile, *Phys. Chem. Chem. Phys.* 15 (2013) 10978–10988.

[43] J.Q. Yan, Y.X. Zhang, S.Z. Liu, G.J. Wu, L.D. Li, N.J. Guan, Facile synthesis of an iron doped rutile TiO₂ photocatalyst for enhanced visible-light-driven water oxidation, *J. Mater. Chem. A* 3 (2015) 21434–21438.

[44] Q. Yang, C. Xie, Z. Xu, Z. Gao, Y. Du, Synthesis of highly active sulfate-promoted rutile titania nanoparticles with a response to visible light, *J. Phys. Chem. B* 109 (2005) 5554–5560.

[45] W.-K. Wang, M. Gao, X. Zhang, M. Fujiitsuka, T. Majima, H.-Q. Yu, One-step synthesis of nonstoichiometric TiO₂ with designed (101) facets for enhanced photocatalytic H₂ evolution, *Appl. Catal. B* 205 (2017) 165–172.

[46] S.R. Barman, D.D. Sarma, Investigation of the L₃-M₄₅M₄₅Auger spectra of Cu, Cu₂O and CuO, *J. Phys. Condens. Matter* 4 (1992) 7607–7616.

[47] N. Pauly, S. Tougaard, F. Yubero, LMM Auger primary excitation spectra of copper, *Surf. Sci.* 630 (2014) 294–299.

[48] P. Unwiset, A. Makdee, K.C. Chanapathaprapol, P. Kidkhunthod, Effect of Cu addition on TiO₂ surface properties and photocatalytic performance: X-ray absorption spectroscopy, *Anal.*, *J. Phys. Chem. Solids* 120 (2018) 231–240.

[49] D. Gao, W. Zhong, Y. Liu, H. Yu, J. Fan, Synergism of tellurium-rich structure and amorphization of NiTe¹⁺ nanodots for efficient photocatalytic H₂-evolution of TiO₂, *Appl. Catal. B* 290 (2021), 120057.

[50] M. Liu, Y. Ji, Y. Li, P. An, J. Zhang, J. Yan, S.F. Liu, Single-atom doping and high-valence state for synergistic enhancement of NiO electrocatalytic water oxidation, *Small* 17 (2021), e2102448.

[51] G. Sadanandam, X. Luo, X. Chen, Y. Bao, K.P. Homewood, Y. Gao, Cu oxide quantum dots loaded TiO₂ nanosheet photocatalyst for highly efficient and robust hydrogen generation, *Appl. Surf. Sci.* 541 (2021), 148687.

[52] L. Le, Y.T. Wu, Z.P. Zhou, H.Y. Wang, R. Xiong, J. Shi, Cu₂O clusters decorated on flower-like TiO₂ nanorod array film for enhanced hydrogen production under solar light irradiation, *J. Photochem. Photobiol.* 351 (2018) 78–86.

[53] A. Marimuthu, J. Zhang, S. Linic, Tuning selectivity in propylene epoxidation by plasmon mediated photo-switching of Cu oxidation state, *Science* 339 (2013) 1590–1593.

[54] G. Vitello, L. Clarizia, W. Abdelraheem, S. Esposito, B. Bonelli, N. Ditaranto, A. Vergara, M. Nadagouda, D.D. Dionysiou, R. Andreozzi, G. Luciani, R. Marotta, Near UV-irradiation of CuO_x-impregnated TiO₂ providing active species for H₂ production through Methanol photoreforming, *ChemCatChem* 11 (2019) 4314–4326.

[55] X. Cheng, Y.H. Li, L.R. Zheng, Y. Yan, Y.F. Zhang, G. Chen, S.R. Sun, J.J. Zhang, Highly active, stable oxidized platinum clusters as electrocatalysts for the hydrogen evolution reaction, *Energy Environ. Sci.* 10 (2017) 2450–2458.